

The Dependence of CGM Physical Properties and Column Density on Halo Mass at z = 0

Andrew W.S. Cook,¹★ Freeke van de Voort,¹

¹Cardiff Hub for Astrophysics Research and Technology, School of Physics and Astronomy, Cardiff University, Queens Building, The Parade, Cardiff, CF24 3AA, UK

Accepted XXX. Received YYY; in original form ZZZ

ABSTRACT

We study the halo mass dependence of the physical properties and column density of the CGM using high resolution cosmological magneto-hydrodynamical ‘zoom-in’ simulations from the Auriga project. We selected a sample of CGM haloes with masses in the range of $10^{10} M_{\odot} < M_{200c} < 10^{12} M_{\odot}$. We analyse the temperature, density, metallicity and radial velocity, with post-processing ions H I, C IV, O VI, Mg II and Si II. The temperature and metallicity of the CGM increase with its mass, with more extended regions of high metallicity in more massive haloes. Furthermore, CGM radial velocity shows that on average inflowing matter dominates in intermediate mass haloes ($10^{11} M_{\odot}$). Column density results agree with observations for high mass haloes ($M_{200c} > 10^{11} M_{\odot}$) at low radii ($R/R_{200c} < 0.4$). These results show that the multiphase nature of the CGM is halo mass dependent and column density of the gas in these simulations are consistent with current theory on collisional and photo-ionisation models.

Key words: Galaxy – Circumgalactic – Galaxy evolution

1 INTRODUCTION

Galaxies are encompassed by a region of diffuse gas that contributes to their formation and evolution. This region of gas - the circumgalactic medium (CGM) - is the gaseous component of dark matter haloes, the product of accreting gas from the intergalactic medium (IGM) and outflowing gas from the interstellar medium (ISM) (Tumlinson et al. 2017).

The CGM is mostly ionised and is a reservoir for baryonic matter and metals (Cen & Ostriker 1999; Werk et al. 2014). The medium combines cool ($T = 10^4 K - 10^5 K$), warm-hot ($T = 10^5 K - 10^7 K$) and hot ($T > 10^7 K$) phases of gas, which describes the CGMs multiphase nature. These various phases of gas temperature means the composition of metal ions within the CGM is diverse, thus impacts the cooling of the halo and accretion onto the galaxy. The density of the CGM follows a decreasing radial profile, remaining constant on average between different haloes as defined by the virial radius (the density of the CGM is equal to 200 times the critical density of the universe). The CGM plays a major role in the evolution of galaxies as it contributes to fuelling star formation by accretion.

Feedback from massive stars driven by stellar evolution and active galactic nuclei (AGN), eject matter from the ISM into the CGM which enriches the environment with metals (Booth & Schaye 2009; Trebitsch et al. 2017; Kimm et al. 2022). Material ejected by these feedback processes could either flow out of the CGM into the IGM and beyond, remain in the CGM or re-accrete onto the galaxy, becoming part of the ISM. This re-accretion is important at late times as it is part of the baryon cycle in the form of wind recycling (Oppenheimer et al. 2010; Hafen et al. 2020; Wright et al. 2021), which is also another contributor to fuelling star formation.

It is possible that the hydrodynamical properties of the CGM not

only depend on feedback from the galaxy, but also on the halo mass (defined as the total mass of gas that is within the virial radius of the CGM, M_{200c}). This relationship would contribute to significant changes in its multiphase nature, implying that dwarf galaxies ($10^{10} M_{\odot} < M_{200c} < 10^{12} M_{\odot}$) could have cooler and lower metallicity CGM than galaxies with $M_{200c} \geq 10^{12} M_{\odot}$ - caused by insufficient stellar feedback due to lower star formation rates (Cedrés et al. 2021) and less dominant, or no, AGN feedback (Eisenreich et al. 2017). It is therefore useful to understand what specific effect M_{200c} has on the CGM properties by analysing the CGM’s dependence on its M_{200c} .

Star forming galaxies ($M_{\star} = 10^{9.3} - 10^{11.6} M_{\odot}$) retain 20-25 per cent of their metals they have ever produced (Peeples et al. 2014) with the rest of their metals mostly removed by outflows thus increasing the metallicity of the CGM and IGM. Surveys such as COS-Halos (Tumlinson et al. 2013; Werk et al. 2013) and COS-Dwarfs (Bordoloi et al. 2014) have studied the column density of galaxies of varying masses. Results from these surveys provide evidence for increasing metallicity with M_{\star} (Prochaska et al. 2017).

The complexity of the CGM means it undergoes many physical processes including gas accretion, galactic winds and cosmic ray feedback. These cannot be treated independently of each other due to their effect on the CGM (Faucher-Giguere & Oh 2023). The CGM also has a range of temperature and densities, leading to its multiphase nature. Simulations have previously probed physical properties such as temperature, density and metallicity with some investigating properties generated in the simulations (Wright et al. 2021; Ramesh et al. 2023) and others deriving physical properties from Voigt profile fitting of synthetic spectra (Appleby et al. 2023). A significant number of observations have been conducted characterising the CGM over the past couple of decades (Anderson & Bregman 2010; Werk et al. 2016; Zahedy et al. 2019). The extended halo can be studied using absorption line spectroscopy (Kraemer et al. 2005; Werk et al. 2014; Lehner et al. 2015; Qu et al. 2022), emission line spectroscopy (Put-

★ E-mail: cookaw@cardiff.ac.uk

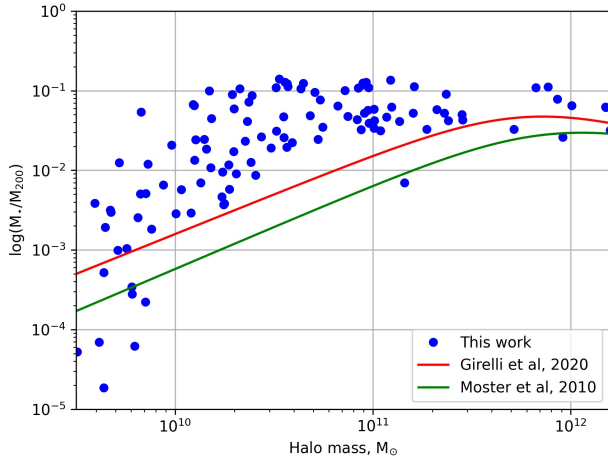


Figure 1. M_*/M_{200c} ratio against M_{200c} . We over plot the double power law using Eq. 2 from Moster et al. (2010) as well as the redshift dependent version which is Eq. 6 in Girelli et al. (2020). Compared to both these models, our simulations have higher M_* than the models predict, with a large scatter at low M_{200c} . This higher M_* and scatter is likely due to the ISM model of our simulations as it is resolved on a subgrid level or the resolution of our simulations.

man et al. 2012; Lopez et al. 2020; Nelson et al. 2023; Truong et al. 2023) or down-the-barrel observations (Rubin et al. 2012). Observations have investigated the covering fraction, as well as equivalent widths of absorption lines (Chen et al. 2023) and column density of the CGM.

Observationally, analysing metal ions can tell us a lot about the properties of the CGM and infer how we model them in simulations (Suresh et al. 2017; Faerman & Werk 2023). Ions ejected from the galaxy can be analysed using modelling to uncover the temperature, metallicity, density and velocity of the CGM (Butsky et al. 2022). Low ionisation states such as H I, Si II, O III and C IV trace cool gas (10^{4-5} K) in the CGM with increasing ionisation states such as O VI and so on generally trace warmer temperatures greater than 10^5 K. The ions O VI, C IV, Mg II and Si II are frequently observed due to their high abundance at low redshifts. These ions trace other physical processes in the haloes such as O VI which traces X-ray emission (Mathur et al. 2021) and cool feedback-driven outflows traced by Mg II and C IV (Cottle et al. 2018).

It is important for us to understand the temperature and density of the CGM to indicate how its multiphase nature changes. Numerical simulations can assist us with suites such as Illustris TNG (Pillepich et al. 2018), EAGLE (Schaye et al. 2015) and NIHAO (Wang et al. 2015) producing cosmological simulations of galaxies and their gaseous environments, with additional code such as TRIDENT (Hummels et al. 2017) available to post process chemistry within simulations. Direct comparisons between simulations and observations can better assist our understanding of the CGM with studies such as Machado et al. 2018 who directly compared simulations of metal fractions in different CGM phases with that of observations, additionally looking at the column density of O VI and Si III.

In this work, we analyse cosmological zoom-in simulations of the CGM to determine the dependence of the density, temperature and metallicity on M_{200c} for haloes with a mass range $10^{10} < M_{200c} < 10^{12}$. Additionally, we compare column densities in our sim-

ulations to observational surveys which includes COS-Halos (Tumlinson et al. 2013; Werk et al. 2016), COS-Dwarfs (Bordoloi et al. 2014) and independent observations (Johnson et al. 2015; Zheng et al. 2023), testing a dependence on stellar mass. We find that the CGM becomes more multiphase in more massive haloes, with an increasing temperature scatter with increasing halo mass. We show that our simulations agree with observed column densities of key ions at high M_* and low radii. Lower mass haloes tend to under-predict column densities the further out from the central CGM you analyse. Our simulated column density agree with observations at impact parameters below 60% the virial radius (R_{200c}) for haloes with $M_{200c} < 10^{11} M_{\odot}$, whereas $M_{200c} \geq 10^{11} M_{\odot}$ are in agreement with observations extending to the virial radius.

We briefly outline the Auriga simulations and their extension to lower masses, including how these haloes are selected in Sec. 2. We will then discuss the physical properties of the CGM in our simulated haloes in Sec. 3. We then discuss results from our column density investigation comparing with the observational data in Sec. 4. Finally, we conclude and discuss links between our results and previous literature in Sec. 5.

2 METHODOLOGY

This work is an extension of the Auriga project - a collection of 30 high-resolution magneto-hydrodynamical (MHD) cosmological zoom-in simulations (Grand et al. 2017). Our work focuses on investigating the CGM around new dwarf galaxies within this simulation suite. We analyse haloes within the halo mass of the CGM, that is the mass of gas within the virial radius (R_{200c}) of the CGM. We study haloes with a halo mass range of $10^{10} < M_{200c} < 10^{12.5} M_{\odot}$ and a stellar mass range of $10^7 < M_* < 10^{11} M_{\odot}$. We select five haloes in this mass range as the primary haloes for analysis. Our goal is to investigate the dependence of the physical properties: temperature, density and metallicity, as well as the column density, of our simulations with M_{200c} .

The simulations were run from $z = 127$ using the finite volume, quasi-lagrangian moving-mesh code AREPO (Springel 2010), which includes MHD and collisionless dynamics (which include particles such as dark matter, stars and black holes). The code uses an unstructured Voronoi mesh following a finite volume with MHD solved by a second order Runge-Kutta integration scheme (Pakmor et al. 2016). The ISM subgrid model in these simulations is described in Springel & Hernquist (2003) as a two-phase medium of dense, cold gas clouds surrounded by hotter, ambient gas. The gas is star forming and thermally unstable once density exceeds the threshold density of $n^* = 0.13 \text{ cm}^{-3}$.

The initial conditions are based on the 100 Mpc^3 volume dark matter only simulation from the EAGLE project (Schaye et al. 2015). Halo selection uses a friends-of-friends (FoF) method at redshift $z = 0$ with a standard linking length (Davis et al. 1985). The high resolution zoom-in region extends to $\sim 5R_{200c}$ of the chosen halo. Auriga adopts cosmological parameters $\Omega_m = 0.307$, $\Omega_b = 0.048$, $\Omega_{\Lambda} = 0.693$ with $H_0 = 100h \text{ km s}^{-1} \text{ Mpc}^{-1}$ where $h = 0.6777$ from Planck Collaboration et al. (2014). These simulations include primordial and metal line-cooling (Vogelsberger et al. 2013; Rahmati et al. 2013) as well as an ultraviolet background with self-shielding (Faucher-Giguère et al. 2009).

Our haloes have a baryonic mass resolution of $\approx 6 \times 10^3 M_{\odot}$ and a dark matter resolution of $\approx 4 \times 10^4 M_{\odot}$. Cells are split in two if the mass within those cells is greater than a factor of two from the target

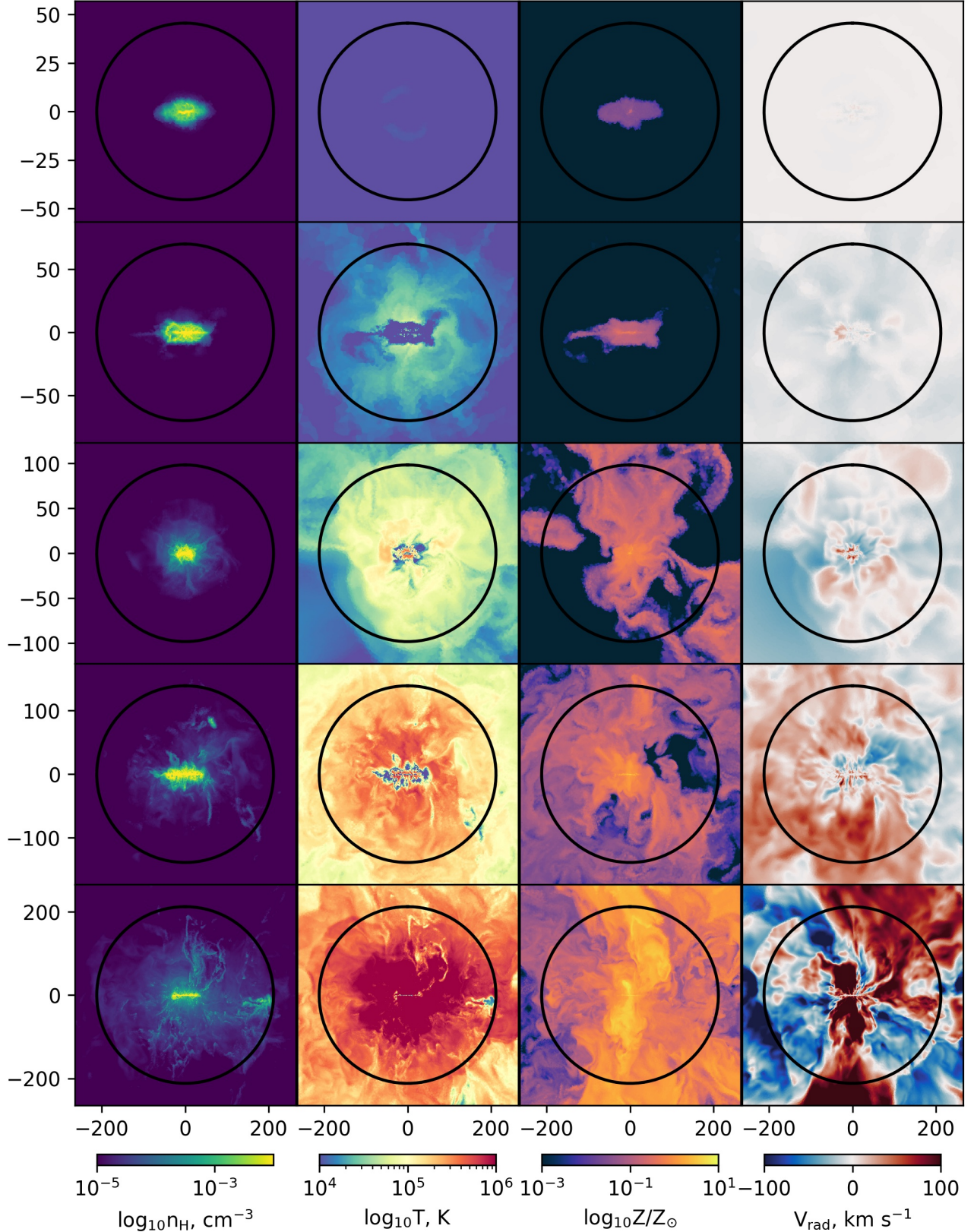


Figure 2. Visualisations of a selection of five haloes edge-on. This shows four properties in each column: hydrogen number density (column 1), temperature (column 2), metallicity (column 3) and radial velocity (column 4). The M_{200c} increases from top to bottom from $10^{9.5} - 10^{12} M_\odot$ in steps of 0.5 dex. The circle in each level shows the virial radius of each halo. Colour maps are fixed to the same limits across all haloes, highlighting major differences between our dwarf haloes and Milky Way mass haloes. Haloes with $M_{200c} < 10^{11} M_\odot$ are cooler, have a smoother distribution of density and lower metallicity than more massive haloes. They are less turbulent as well with less outflows from the centre. As M_{200c} increases, so too does the multiphase nature of the CGM with greater differences in the temperature and density in the same haloes.

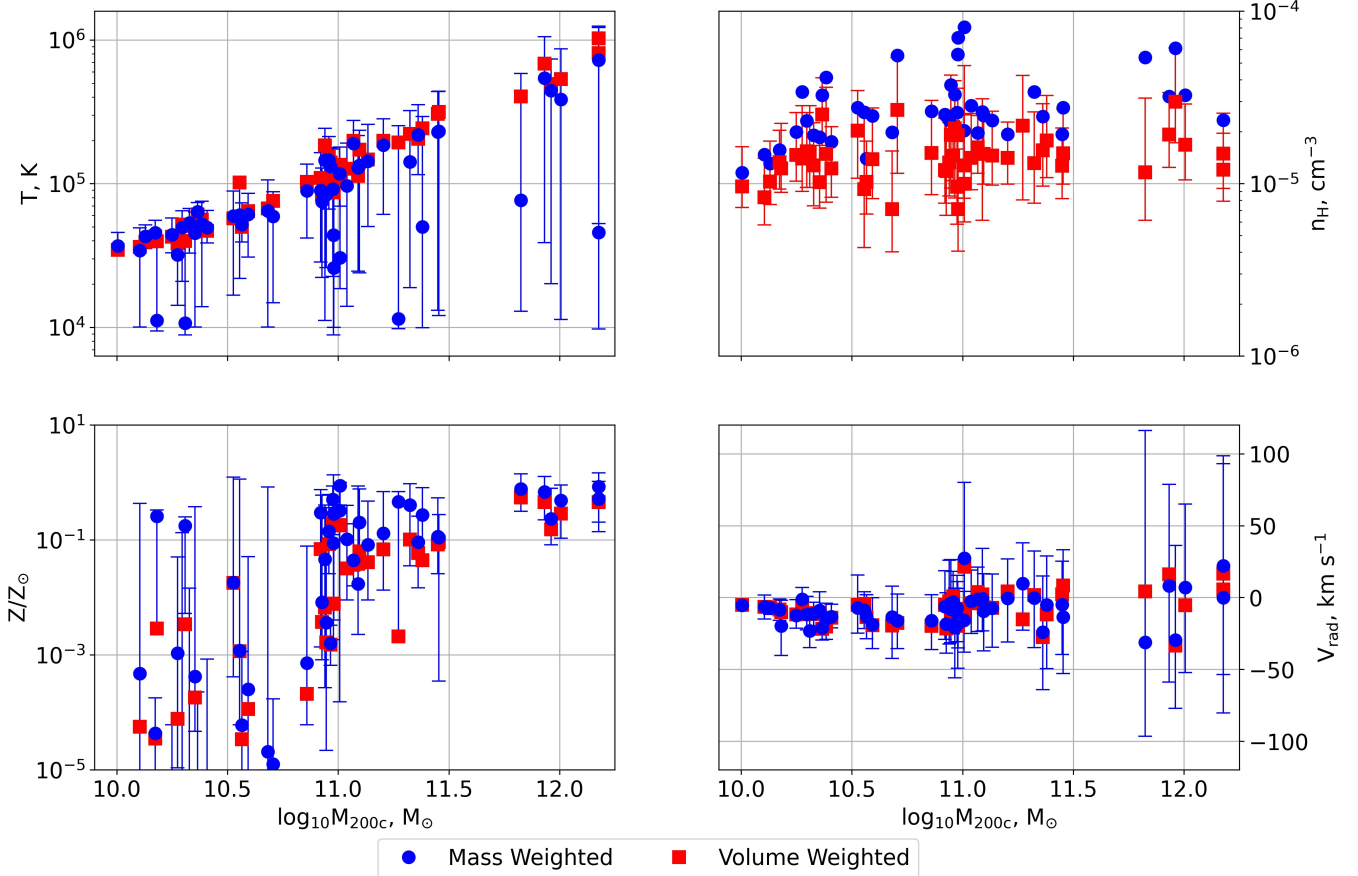


Figure 3. Median temperature (top, left), hydrogen number density (top, right), metallicity (bottom, left) and radial velocity (bottom, right) against M_{200c} with 16th and 84th percentile scatter. Median and scatter are measured between $0.3 \leq R/R_{200c} \leq 1.0$ to account for the dominant high density and cool temperature of the central CGM. Mass weighted quantities are in blue and volume weighted quantities are in red. Weightings we focus on include errorbars of the same colour, additional weights are added for clarity. The median and scatter of temperature and metallicity increases with halo mass. This shows that at higher M_{200c} , up to $10^{12} M_\odot$, CGM gas is more multiphase with greater scatter in temperature. The density of these haloes is consistent across all halo masses with no clear dependence on the halo mass. There is also very little dependence on the radial velocity with halo mass but generally the CGM is dominated by inflowing gas with outflows beginning to dominate above $M_{200c} = 10^{12} M_\odot$.

baryon mass resolution and are similarly merged if their mass is less than two times the mass resolution.

The galaxy formation model in Auriga is described fully in [Grand et al. \(2017\)](#) and summarised here. Auriga uses a physics model which incorporates feedback from SN and active galactic nuclei (AGN), and star formation. Stellar feedback is a stochastic process which is the product of wind particles being ejected from star-forming gas, temporarily decoupled from hydrodynamic interactions until reaching 5% of n^* . Temperature in these simulations has a thermal floor applied meaning temperature does not go below 10^4 K. This is due to inefficient cooling below this temperature as well as cooling based on molecular clouds which Auriga does not resolve.

AGN feedback is a dual-phase process including a radio and quasar mode. The radio mode heats bubbles of gas at a size of $0.1 R_{200c}$ at random locations following the inverse square law up to $0.8R_{200c}$. The quasar mode injects energy isotropically into neighbouring gas cells. BH are seeded in the simulations with a mass of $10^5 M_\odot$ when the FoF halo group has a mass $M_{\text{FoF}} \geq 10^{10} M_\odot$. This means BH will not be seeded in our dwarf haloes and thus will be dominated by stellar feedback. For the purposes of this research, we remove gas cells from our simulations which are star-forming in post-processing.

This removes the ISM from our results as it is a subgrid model and therefore not resolved.

Additionally, this paper analyses the column density of our simulations. We chose ions that have a lot of observational data to compare against and trace numerous physical properties. These include H I and four metal ions: Mg II, Si II, C IV and O VI and compare with observations. Column density of H I is calculated on-the-fly where the metals are calculated in post-processing using an interpolation method. We use ion tables generated with CLOUDY ([Ferland et al. 2017](#)) used in [Hummer et al. \(2017\)](#) to compute the number density of our metals. This method depends on the temperature, redshift and hydrogen number density of the gas and interpolates with the ion tables, giving us the number densities of the metals. We can then use this number density to calculate the ion column density. These ions were chosen, because of the relatively large amount of observational data available ([Fox et al. 2005; Ranjan et al. 2022](#)).

Figure 1 shows the ratio of M_\star to M_{200c} as a function of M_{200c} . We find our simulations produce an overestimate for M_\star when compared to models from [Moster et al. \(2010\)](#) and [Girelli et al. \(2020\)](#) but still follow a linear trend above $10^{10} M_\odot$. Furthermore, Table A1 lists key properties of the 30 largest haloes. We choose Au0_10,

Au9_10, Au0_11, Au4_11 and Au6_12 which range in halo mass from $10^{10} - 10^{12}$ in steps of $10^{0.5}$ within the portion of Figure 1 that best follows prior models.

3 DEPENDENCE OF PHYSICAL PROPERTIES IN THE CGM ON HALO MASS

We present results from our investigation into the halo mass dependence of the physical properties of the CGM. We analyse these properties via two methods: (1) by taking the median of the whole CGM with its 16th and 84th percentiles and (2) by taking the median and 16th and 84th percentile across the radius of the CGM. For the first case we compare the median and scatter of all our haloes with their halo mass and for the second case, select five haloes for the radial profiles, taking halo masses that are 0.5 dex apart from each other. We analyse the temperature, density, metallicity and radial velocity of these haloes between $0.3R_{200c}$ and $1R_{200c}$ to account for the dominant cool and dense centre of the CGM. We mass-weigh temperature, metallicity and radial velocity, and volume-weigh density.

3.1 Median Properties

Figure 3 shows median temperature consistently at 10^4 K in lower mass haloes ($10^{10} < M_{200c} < 10^{11.5} M_\odot$) due to more efficient cooling from higher density and higher metallicity as shown in Figure 2. As halo mass increases, temperature scatter increases from ~ 0.5 dex in lowest mass haloes ($10^{10} M_\odot$) up to scatter of ~ 2 dex at high masses ($10^{12} M_\odot$). As these galaxies are larger, they are prone to stronger shocks at the virial radius as well as stronger feedback which contributes to increased heating. The scatter of the CGM temperature describes how multiphase the medium is. As the scatter increases with halo mass, we infer that the multiphase nature is halo mass dependent.

We see no clear dependence of the median density or its scatter on halo mass for this selection. This is due to average density being independent of halo mass by definition of the virial radius. Scatter of density does fluctuate slightly within our errors. As we have some satellites in these simulations this may be a primary factor.

The median metallicity of our haloes increases linearly with M_{200c} whereas its scatter decreases. The scatter decreases from > 4 down to 0.3 dex, demonstrating higher metallicity in more massive haloes. As more massive haloes have a higher stellar mass and stronger feedback contribution from AGN, this causes the CGM to become more enriched with metals. This is seen in Figure 2 where the metallicity extends further out into the CGM, with more collimated outflows perpendicular to the inner CGM. Row 1 and 2 of Figure 2 show a concentrated region of metals in the centre of the halo, largely contributed from the stellar feedback of the galaxy. Errors are large for low-mass haloes as the outer CGM will contain very low abundances of metals.

Halo with a halo mass above $\sim 10^{10} M_\odot$ are dominated by inflowing gas as the central CGM starts accreting more matter. This is because when $M_{200c} > 10^9 M_\odot$ galaxy formation begins with accretion flowing onto the centre (Okamoto et al. 2008). Additionally, these haloes do not have as strong stellar feedback and significantly weaker AGN feedback than larger haloes. As the halo mass increases, these dominant inflows begin to turn into outflows which can be seen at $M_{200c} > 10^{12} M_\odot$. This is where stronger feedback from AGN begins to dominate over the stellar feedback, as well as ejecting more matter out than is being accreted. However, our AGN feedback model

does not produce jets so this is likely caused by additional energy being injected into mostly outflowing pockets.

3.2 Radial Profiles

Figure 4 shows the radial dependence of these properties for six haloes of increasing M_{200c} . As M_{200c} increases, the median and scatter of temperature increases with higher median values seen in more massive haloes. The temperature has an extended region of 10^4 K gas out to anywhere between $0.05 - 0.25R/R_{200c}$ which demonstrates the disk at the centre of the CGM. Sharp increase in temperature is seen past this radius which increases to or exceeds the virial temperature and decreases linearly with radius.

In dwarf haloes ($M_{200c} = 10^{10} \& 10^{10.5} M_\odot$), temperature has little to no scatter across its radius. Their metallicity is less extended than more massive haloes which could be caused by lack of strong outflows.

In more massive haloes ($M_{200c} = 10^{11}, 10^{11.5}, 10^{12}$) there is greater scatter at larger radii due to stronger outflows from the galaxy, including feedback from AGN and SN. These outflows eject metals from the ISM, enriching the CGM and allowing it to cool more efficiently. The greater scatter in temperature can be attributed to the virial temperature which these haloes reach and then rapidly cool down to 10^4 K.

The metallicity does not extend far in our lower mass haloes ($10^{10} - 10^{10.5} M_\odot$) not extending much past $0.4R_{200c}$. The highest metallicity in these haloes is in the centre where most metals are being produced. Due to weak stellar feedback, the metals cannot extend much past the inner disk, with the additional metallicity readings < 0.1 the product of inflowing matter. As the halo mass increases, metallicity extends further with additional support from stronger stellar feedback. Reaching $M_{200c} = 10^{12} M_\odot$ also means AGN feedback begins to get stronger, increasing the distribution of metals into the outer CGM, hence the higher lower bound than the previous haloes.

These results indicate the multiphase nature of the CGM is dependent on its halo mass. This is due to the increased scatter from ~ 0.05 to ~ 2 as M_{200c} increases. These haloes have significantly lower metallicity in their CGM due to weaker stellar feedback. It has been previously shown that the metallicity of accreting gas in haloes with $M_{200c} = 10^{12} - 10^{12.5} M_\odot$ is high and grows steadily in time (Rubin et al. 2012; Wright et al. 2021). We find that haloes within this mass range and down to $\sim 10^{11.5} M_\odot$ are dominated by accreting gas and have high metallicities across the radius of the CGM.

4 COLUMN DENSITY OF THE CGM

We compare the column density of various ions in our simulations with the following selection of observational data: Bordoloi et al. (2014); Werk et al. (2013); Tumlinson et al. (2013); Johnson et al. (2015); and Zheng et al. (2023). Column density is dependent on the ionising mechanism of the CGM which is dependent on temperature and density (Strawn et al. 2023). This can either be collisional or photo-ionisation equilibrium (CIE/PIE respectively) which occur at different temperatures. It is for this reason we define two temperature regimes: the warm regime which is traced by C IV and O VI at temperatures of $T = 10^{5.0} - 10^{5.5}$ K for collisional ionisation and $T = 10^{4.0} - 10^{4.5}$ K for photo-ionisation, and a cool regime, traced by H I, Mg II and Si II at temperatures of $T = 10^{4.0} - 10^{4.1}$ K for both collisional and photo-ionisation.

Figure 5 shows edge-on images of the (from top to bottom) H I,

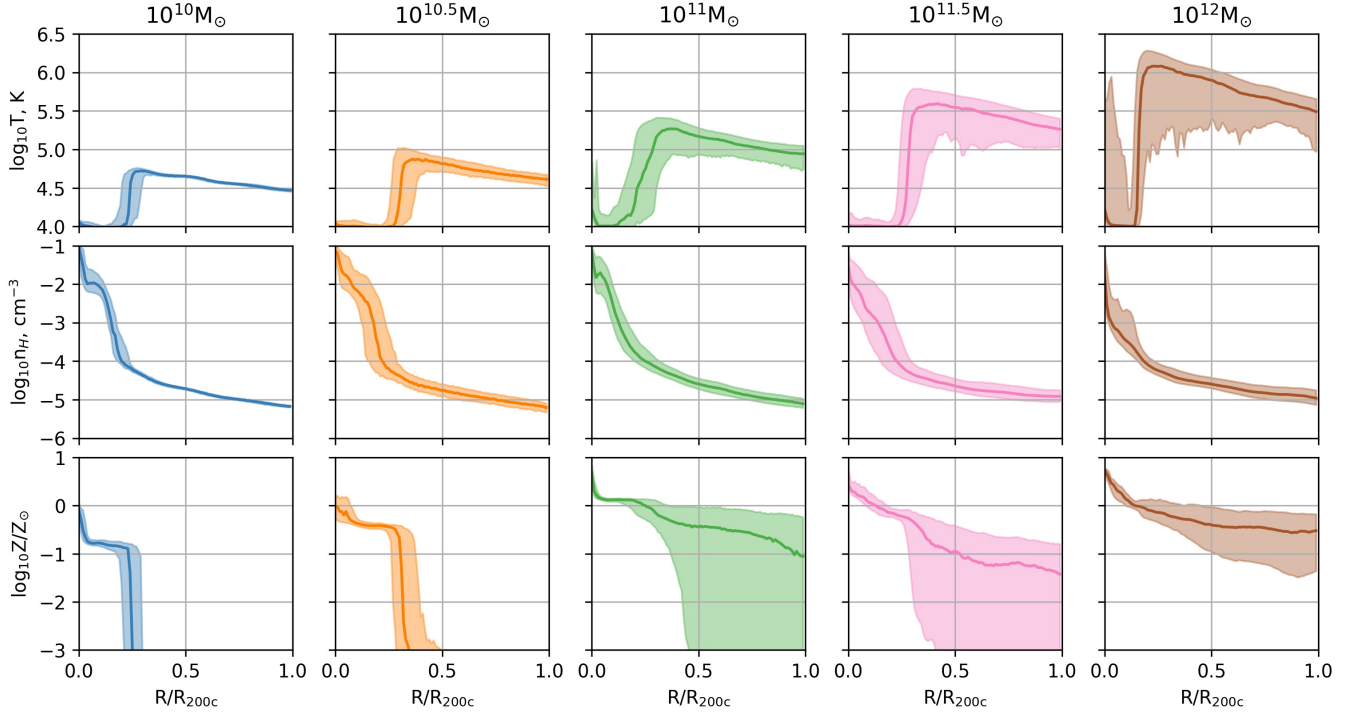


Figure 4. Normalised radial profile of CGM properties. Each column corresponds to one halo selected at each halo mass, ranging in M_{200c} from $10^{10} < M_{200c} < 10^{12} M_\odot$ in steps of 0.5 dex. Each panel shows the median temperature (top), density (middle) and metallicity (bottom) with the 16th and 84th percentile scatter. Temperature and metallicity are mass weighted whereas density is volume weighted. The structure of these haloes can be determined in these radial profiles, with $10^4 K$ gas extending to anywhere from 0.05 – 0.25 R_{200c} . Median metallicity is seen to extend further out in haloes of increasing halo mass due to stronger outflows from the central galaxy.

$\text{C}\,\text{IV}$, $\text{O}\,\text{VI}$, $\text{Mg}\,\text{II}$ and $\text{Si}\,\text{II}$ column density for the same five haloes as in Figure 2. These are organised in increasing M_\star from left to right $10^7 - 10^{11} M_\odot$, corresponding to a M_{200c} of $10^{10} - 10^{12} M_\odot$. $\text{H}\,\text{I}$, $\text{Si}\,\text{II}$ and $\text{Mg}\,\text{II}$, probing the cooler phase, show substantially higher column densities close to the centre of all haloes. Below $M_{200c} < 10^{11} M_\odot$, metals are confined to the centre of the CGM with this being the coolest part of the CGM. Above $M_{200c} \geq 10^{11} M_\odot$, stronger outflows distribute metals out to and beyond R_{200c} . These cooler ions also show filamentary structure, similar to the underlying density structure of their CGM as shown in Fig 2.

For $\text{C}\,\text{IV}$ and $\text{O}\,\text{VI}$, probing the warm-hot phase, these extend further into the CGM in all directions above $M_{200c} \geq 10^{11} M_\odot$ which would similarly be because of stronger outflows distributing the metals. Due to a greater, extended temperature scatter, as shown in panel 1 of Fig. 3 and 1st row of Fig. 4, $\text{C}\,\text{IV}$ and $\text{O}\,\text{VI}$ exists in regions where $\text{H}\,\text{I}$, $\text{Si}\,\text{II}$ and $\text{Mg}\,\text{II}$ wouldn't. Additionally, $\text{C}\,\text{IV}$ and $\text{O}\,\text{VI}$ do not reproduce the filamentary structure observed in the other three ions. This is indicative that the filaments formed by $\text{H}\,\text{I}$, $\text{Si}\,\text{II}$ and $\text{Mg}\,\text{II}$ are significantly cooler than the general structure of the CGM. Low column densities are found in the centre of the CGM, caused by photo ionisation. The metal distribution of these more massive haloes and higher temperatures means these ions extend to further radii with increasing M_{200c} . This will reach a limit at around $10^7 K$ at which point Bremsstrahlung radiation occurs, completely ionising atoms.

4.1 Average Column Density

Figure 6 shows the median column density with scatter of the 16th and 84th percentile averaged over three axes (one face-on and two edge-on). We take the median of our simulations between $0.0 - 0.6R_{200c}$ in bins of 0.2dex as observational data we compare to has impact parameters below this. The increase in column density with M_\star we find in our simulations are matched by a similar increase in the observational data. Most of our results match observations at high M_\star values with most of the observational data lying within our 1σ scatter. In lower mass haloes we find the scatter in our data falls within upper limit values in the observational data. In all regimes, at high M_\star , we find that our simulations match observations for high M_\star but are underpredicted at stellar masses below $M_\star \approx 10^{9.7}$.

Our simulations produce $\text{H}\,\text{I}$ column density on-the-fly, following a decreasing radial trend. We see similar medians for all haloes above $0.2R_{200c}$ independent of M_\star . Higher average abundances of $\text{H}\,\text{I}$ is found within $0.2R_{200c}$ at higher stellar masses. This would be the region where the coldest gas would be.

$\text{O}\,\text{VI}$ and $\text{C}\,\text{IV}$ decrease with radius below stellar masses of $10^{10} M_\odot$. $\text{O}\,\text{VI}$ is commonly an indicator of $T \approx 10^{5.5} K$ for haloes with $M_\star > 10^{10}$ if it is produced through collisional ionisation which would explain the larger column density in higher stellar mass haloes. Below this mass, photo-ionisation dominates, meaning we see less $\text{O}\,\text{VI}$ as it requires more energy to excite atoms of oxygen.

$\text{C}\,\text{IV}$ follows a linear increase in column density within the inner $0.2R_{200c}$ as stellar mass increases. This decreases as radius increases for stellar masses of $< 10^{10}$. The dominating UV background that occurs in low mass haloes, typically $M_\star < 10^{10} M_\odot$, causes photo-

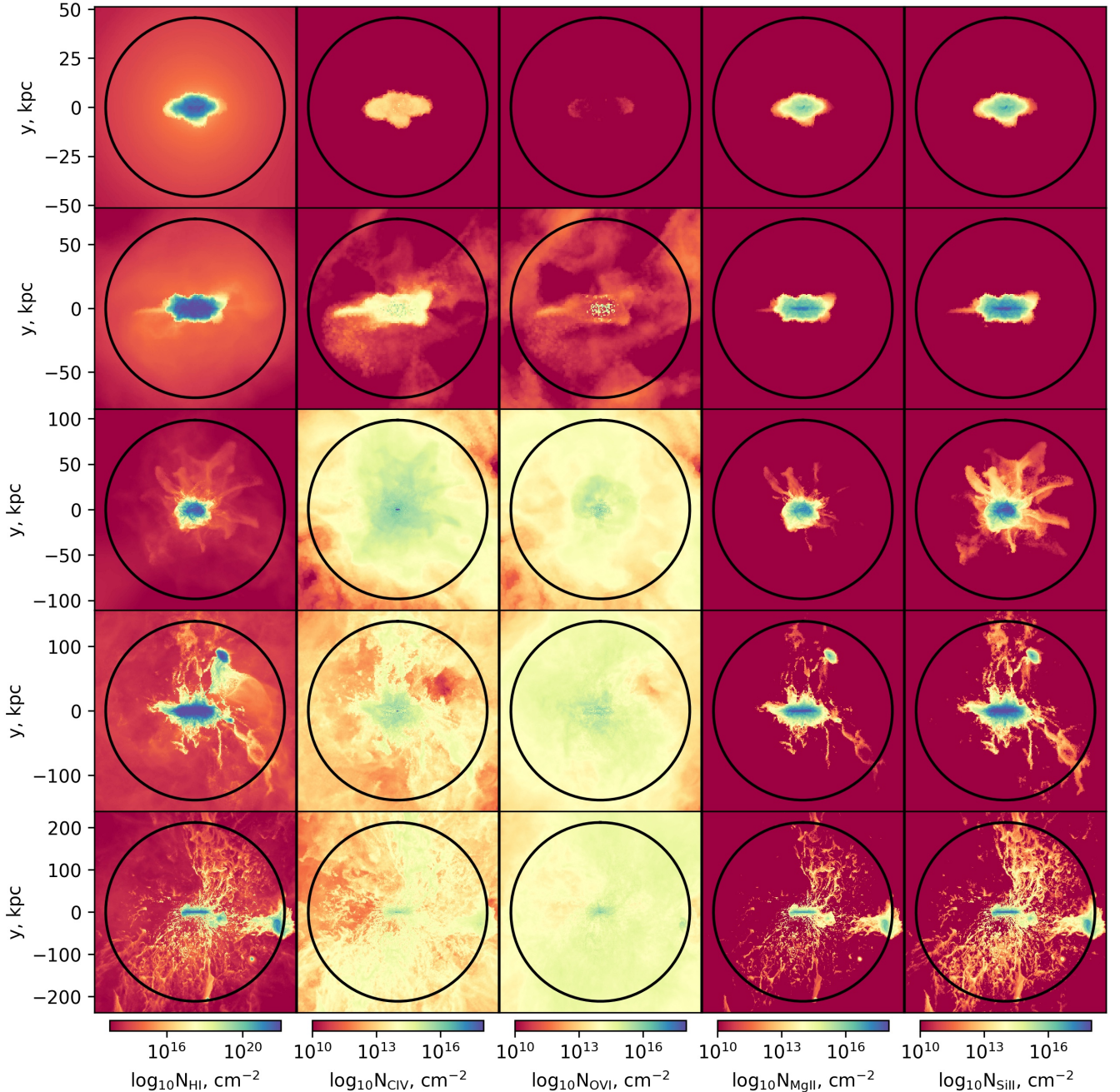


Figure 5. Visualisation of column densities across multiple haloes taken edge-on to the galaxy, with each halo laid out the same way as in Fig. 2. Each column is H I (left column), C IV (2nd column), O VI (3rd column), Mg II (4th column), Si II (right column). The virial radius of each halo is indicated by the black circle. Stronger stellar feedback tied with greater scatter in temperature means we see more extended column density of C IV and O VI in haloes with masses $\geq 10^{11} M_\odot$. Additionally, some slightly more extended column density of H I, Mg II and Si II as well. Smaller haloes ($M_{200c} < 10^{11} M_\odot$) lack C IV and O VI due to their significantly lower temperatures and outflows. H I, Mg II and Si II are found mostly in the cool, dense centres of the haloes.

ionisation of atoms. The range of temperatures and densities from Strawn et al. (2023) for CIV is $10^4 - 10^{4.5} \text{ K}$ and $10^{-6} - 10^{-4} \text{ cm}^{-2}$. Typically this is the common temperature and density ranges of the inner CGM, consistently remaining at $\sim 10^4 \text{ K}$ as in Fig. 3.

Mg II and Si II are found in the inner CGM of $M_{200c} < 10^{11} M_\odot$ haloes. More massive haloes have these ions in their outer CGM due to stronger feedback from stars and AGN, expelling metals further into the outer CGM. Moreover, as most of the gas is too hot $> 10^6 \text{ K}$

Mg II and Si II will be in higher ionisation states. This means their column densities in the outer CGM drop off quickly for Mg II and Si II. H I peaks in the centre sharply decreasing and plateauing to 10^{14} cm^{-2} .

Observationally, the line-of-sight velocity range more than likely goes far beyond the radius of the CGM. This means additional column density is measured for ions outside of the halo. Our simulations only

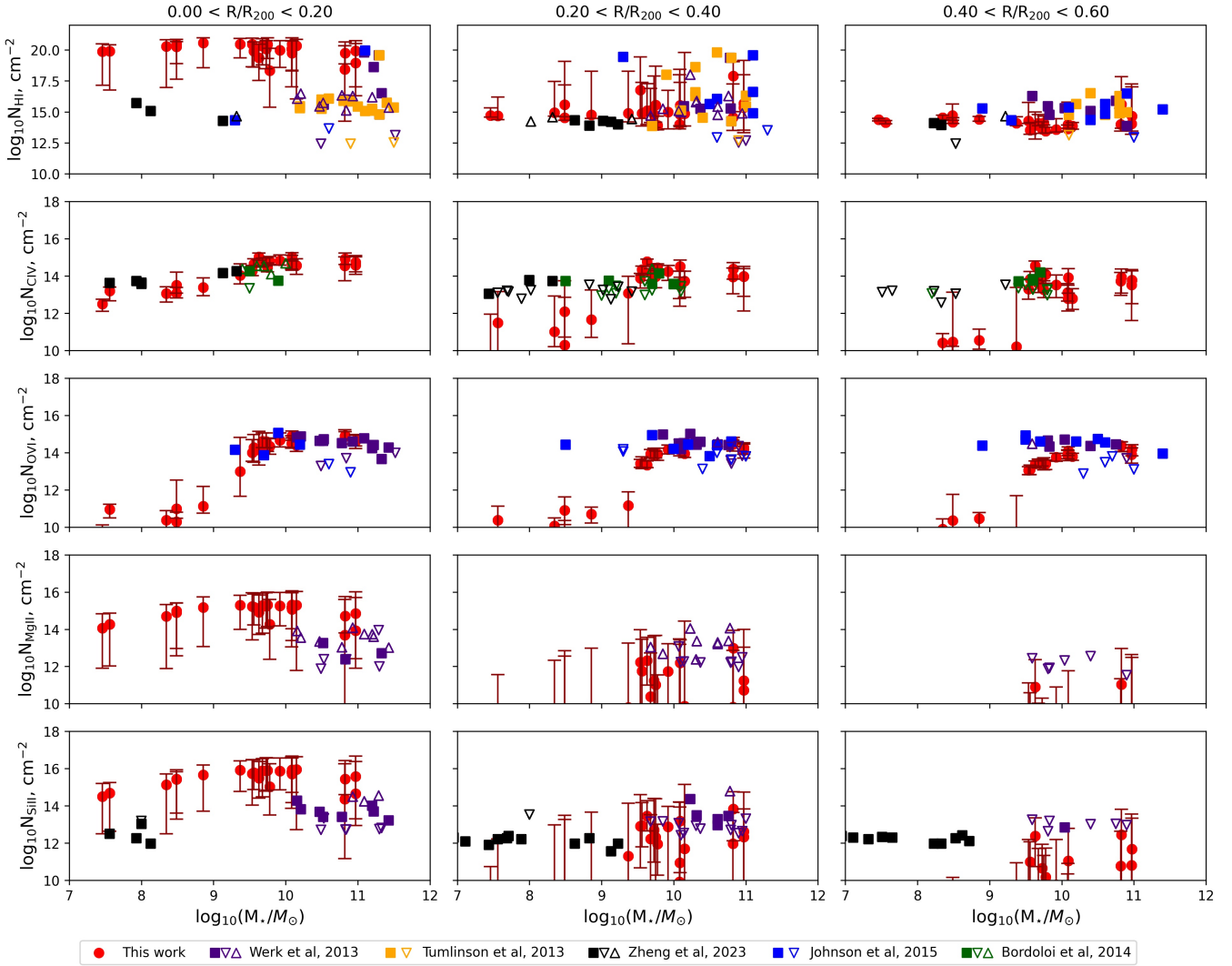


Figure 6. Median column density of each halo. Red points are median values with scatter bars showing the 16th and 84th percentile against M_{\star} . The column density is measured within $0.6R_{200c}$ simulations in radial bins of $0.2R_{200c}$. The line-of-sight extends to the virial radius and a median is taken along three different directions, two edge-on and one face-on projections. Each panel shows H I (1st row), C IV (2nd row), O VI (3rd row), Si II (4th row) and Mg II (5th row). Additionally, we compare with observational data as indicated in the legend (Werk et al. 2013; Tumlinson et al. 2013; Bordoloi et al. 2014; Johnson et al. 2015; Zheng et al. 2023). Detections are shown as filled squares and upper (lower) limits as empty downwards (up) arrows. The observational error bars are omitted for readability. N_{HI} from our simulations agree with observations across all M_{\star} . We find that the ion column densities predicted by our simulations agree with observations at high M_{\star} and low radii. Mg II and Si II column densities are higher in more haloes within $0.2R_{200c}$, as this area is dominated by $\sim 10^4 \text{ K}$ gas. Our results overestimate H I for the inner $0.2R_{200c}$ due to the ISM being dominant within this region. Outside of $0.2R_{200c}$, column density of H I plateaus to 10^{13} cm^{-2} , in agreement with observations.

measure along a line-of-sight that is within the virial radius of the CGM.

4.2 Radial Profile

Figure 7 shows the various column densities of our haloes as a function of radius compared with observational data. We binned each column by stellar mass with bins having a range of 0.75dex. The columns include observational data from Werk et al. (2013); Tumlinson et al. (2013); Bordoloi et al. (2014); Johnson et al. (2015); Zheng et al. (2023) that falls within the range of those stellar mass bins. Each halo selection from our simulations lies at the lower end of the bin range.

Scatter in H I column density as a function of radius increases with stellar mass with larger ranges of measured column density in the outer CGM. As shown in Figure 3, the scatter in CGM temperature increases with M_{200c} . H I column density is higher in more massive objects due to more variations in temperature and larger volumes which allows for more H I to take up more space. We see good agreement between our H I results and that of observations which mostly follow the decreasing radial profile of H I with more massive haloes having more H I at higher column density further out in the CGM. The ions probing the warm-hot regime (C IV and O VI) have high column densities in haloes with $M_{200c} \geq 10^{11} M_{\odot}$ or M_{\star} of $\sim 10^{9.8} M_{\odot}$. C IV and O VI column density remains above $\sim 10^{13} \text{ cm}^{-2}$ in the outer CGM of these haloes. As the outflows in these haloes are

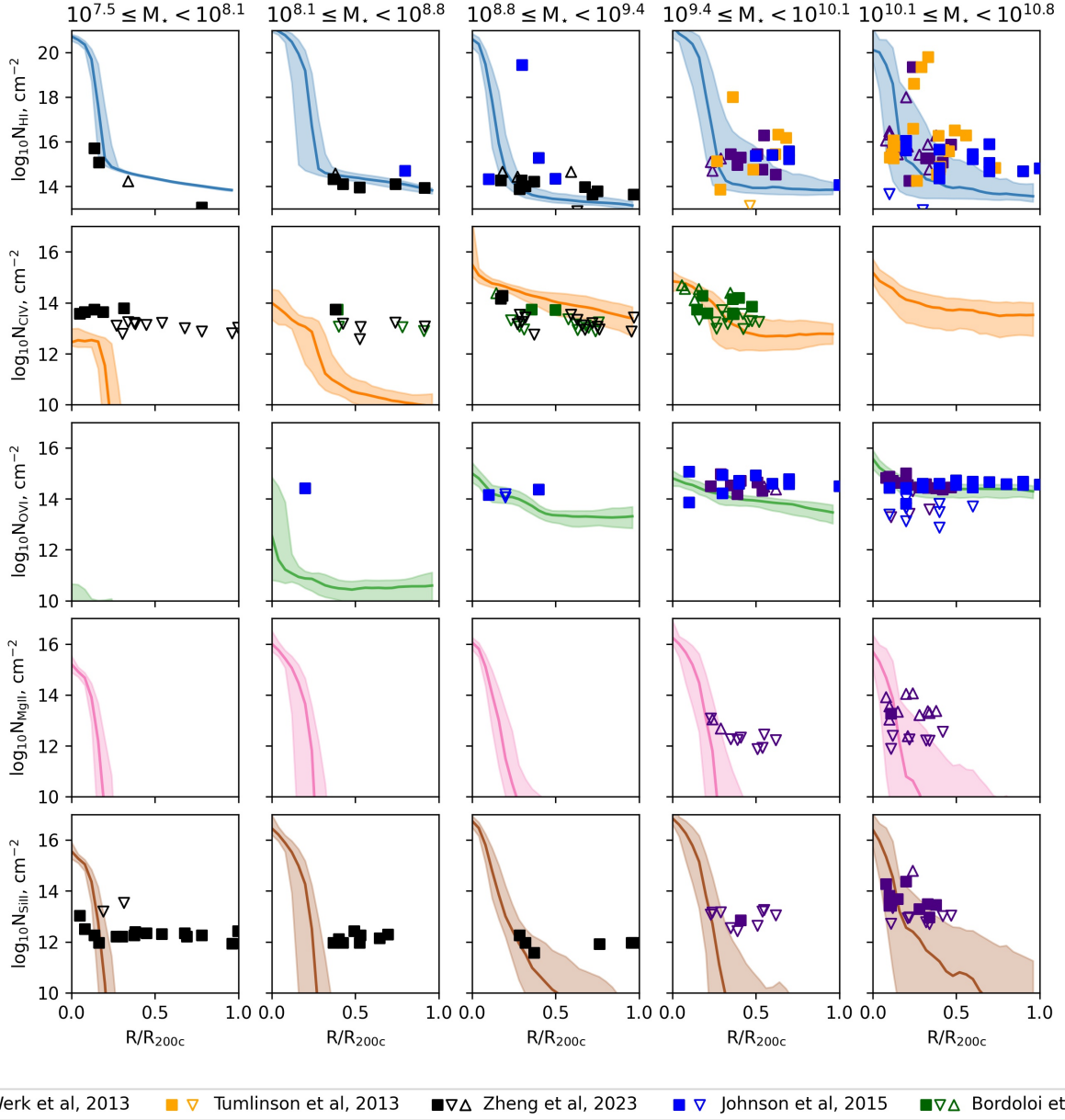


Figure 7. Column density against radius normalised by R_{200c} . Structure of this figure is organised the same as in Figure 5 using the same selection of haloes. Each panel includes the median column density across the radius with its 16th and 84th percentile scatter. Observational data is binned to be within $10^{7.5} < M_* < 10^{11} M_\odot$ in equal intervals of 0.7 dex. H_I reliably matches observations with in both median and scatter in low mass and high mass haloes. C_{IV} and O_{VI} agrees with haloes at $M_{200c} \geq 10^{11} M_\odot$. C_{IV} in haloes $M_{200c} < 10^{11} M_\odot$ drops to significantly low levels at lower radii which is in agreement with the upper limits of observations. Mg_{II} and Si_{II} agrees with observations at lower radii as our simulations have a steep drop off in their column density.

stronger, metal enrichment extends to greater radii. With temperature also being more multiphase in these haloes, we see higher column density in the outer CGM. Below $10^{11} M_\odot$, there is a steep drop off in C_{IV} column density outside of $0.25 - 0.3R_{200c}$ to values of $N_{CIV} < 10^{13} \text{ cm}^{-2}$. Observations have upper limits for the column density in for these haloes of around 10^{13} which indicates our data agrees with the upper limits of observations of C_{IV}. O_{VI} column density has significantly lower column density below $10^{11} M_\odot$ with most of our data found below 10^{12} cm^{-2} .

For the cool regime, column densities begin high and drop rapidly around $\sim 0.4R_{200c}$ for both Mg_{II} and Si_{II}. In lower mass

($\leq 10^{11} M_\odot$) haloes, we have a large amount of data from Zheng et al. (2023) which suggests nominal column density readings for this stellar mass range out to the virial radius of the CGM. This is due to intervening matter along the line-of-sight of the observations which causes column density to not dip below 10^{12} cm^{-2} . As halo mass increases $\geq 10^{11} M_\odot$, Mg_{II} and Si_{II} have more extended column density with Si_{II} showing even higher column density than Mg_{II}. Haloes of mass $\geq 10^{11} M_\odot$ agree with nominal observational results or at least their upper limits.

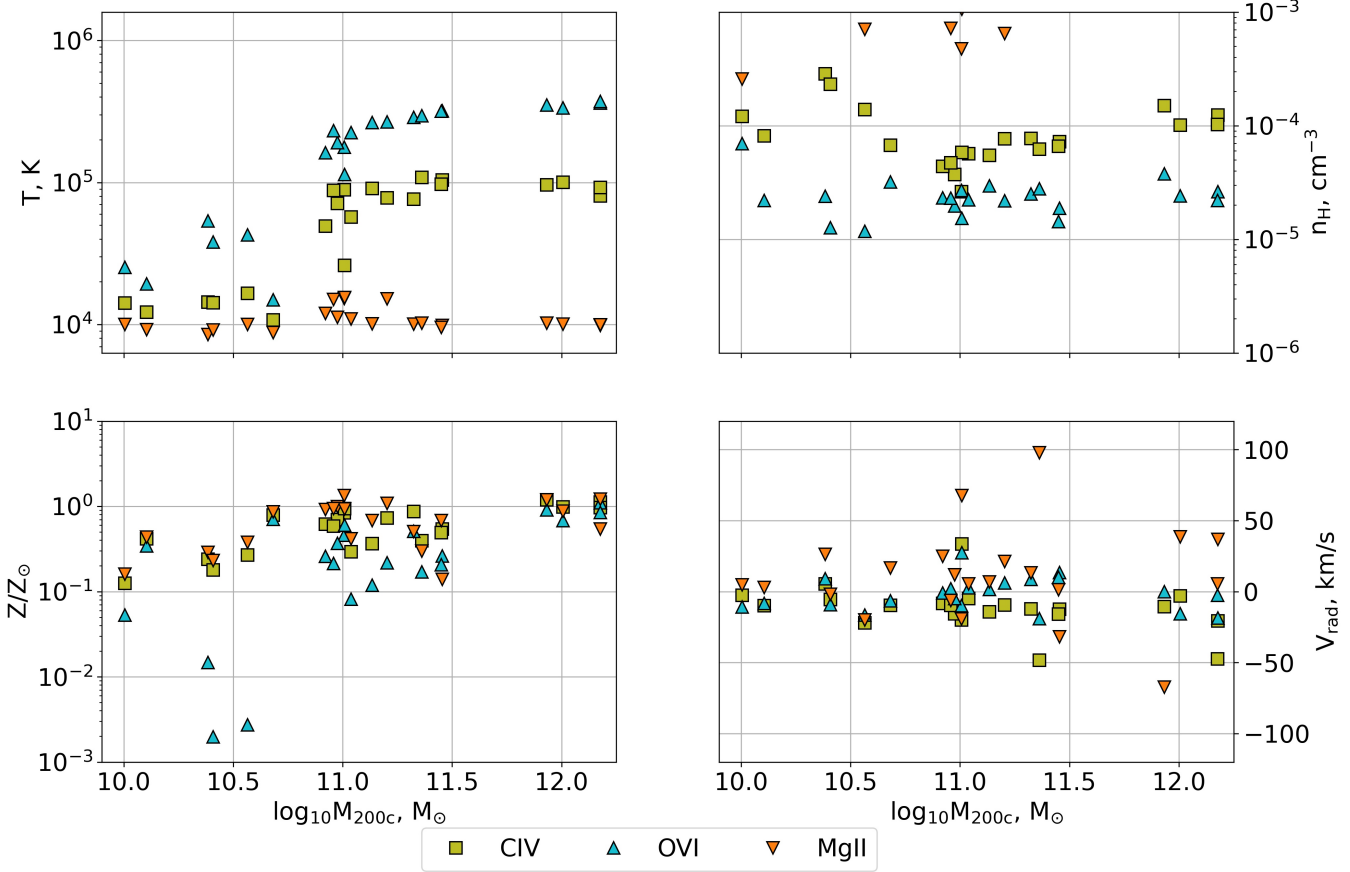


Figure 8. Median temperature (top, left), hydrogen number density (top, right), metallicity (bottom, left) and radial velocity (bottom, right) against M_{200c} as in Fig. 3. Each property is weighed by ion mass of C_{IV}, O_{VI} and Mg_{II} and measured between $0.3 \leq R/R_{200c} \leq 1.0$. Error bars are omitted from this plot for clarity. Median temperature of C_{IV} and O_{VI} are seen to increase once $M_{200c} = 10^{11} M_\odot$ which indicates a boundary between photo and collisional ionisation. Temperatures for C_{IV} and O_{VI} agree with current theory of CIE of $\sim 10^5$ K and $\sim 10^{5.5}$ K respectively. For $M_{200c} < 10^{11} M_\odot$, these ions are excited via photo-ionisation equilibrium according to our models, indicating their temperature is $\sim 10^{4.5}$ K. Mg_{II} remains consistently at 10^4 K no matter the halo mass as well as demonstrating high densities, indicating it is mostly found in the central CGM.

4.3 Relation to Physical Properties

Figure 8 shows the physical properties as in Figure 3 now weighed by the mass of C_{IV}, O_{VI} and Mg_{II}. H_I and Si_{II} are omitted as results between these and Mg_{II} are similar for all properties. Additionally, we measured the median values of these properties between $0.3 \leq R/R_{200c} \leq 1.0$ excluding the dominant central CGM.

We see a distinct change in temperature between C_{IV} and O_{VI} at $M_{200c} = 10^{11} M_\odot$. C_{IV} and O_{VI} are at temperatures which correspond to their CIE values above this halo mass. Temperature and density of C_{IV} and O_{VI} is $\sim 10^5$ K, $\sim 10^{-4}$ cm⁻³ and ~ 5.5 K, $\sim 10^{-4.8}$ cm⁻³ respectively. This is consistent with Strawn et al. (2023) (Fig. 1) which specifies a temperature range for photo-ionisation equilibrium of $10^2 - 10^{4.5}$ K for both C_{IV} and O_{VI} with densities ranging from $10^{-6} - 10^{-4}$ cm⁻³ for C_{IV} and $10^{-7} - 10^{-5}$ cm⁻³ for O_{VI}.

Mg_{II}, along with H_I and Si_{II}, remain at cool temperatures of $\sim 10^4$ K as well as densities of $\sim 10^{-1}$ across the range of halo masses. These ions accumulate in the coolest and densest parts of the outer 70% of the CGM, with the majority mostly residing in the centre of the CGM where it is the coolest and densest. Average metallicity remains at similar values across the range of halo masses.

Metallicity of these haloes increases linearly with halo mass with some outliers in O_{VI} around $\sim 10^{10.5} M_\odot$.

We find varied results between our simulations and observations. Our simulations are in agreement with observational detections in the warm regime across the radius of the CGM at high stellar masses. We find more reliable agreement in the cool regime within $0.2R_{200c}$ where most cool gas is found and the ISM dominates. At larger stellar masses ($> 10^9$) above $0.2R_{200c}$, the cool regime is still in agreement with observational upper limits.

Similar results were found in Illustris TNG50 where Nelson et al. (2021) found that the central ~ 10 kpc is where most Mg_{II} exists. This study shows that for haloes larger than ours ($10^{13} - 10^{13.5} M_\odot$) the presence of Mg_{II} increases monotonically with halo mass with flatter radial profiles. Appleby et al. (2023) show that absorption of H_I can occur in any phase of the CGM, including condensed, diffuse, hot or the warm-hot intergalactic medium (WHIM). Condensed gas constitutes to the majority ($\sim 100\%$) of the absorption of H_I and low metal ions, and around 87% of all C_{IV}. O_{VI} is mostly prevalent in gas from either hot gas or WHIM, indicating it mostly inflows from the IGM. Our results are in agreement with this as H_I matches observations across a wide range of M_\star with C_{IV} only being present in dwarf haloes close to the centre and statistically significant amounts

of O VI occurring at larger radii in larger haloes, with 8 demonstrating how O VI mostly inflows in the outer CGM.

Mina et al. (2021) also obtained similar results to our dwarf galaxies with simulations of dwarf galaxies with $M_\star = 10^7 - 10^8 M_\odot$ that produce O VI column densities $> 10^{13.5} \text{ cm}^{-2}$ and less extended Si II and C IV only out to about 0.2–0.3 R_{200c} . We see similarities between this and our results as shown in Figure 6 where at low M_\star the column density for C IV and Si II drop off much sooner than more massive haloes.

Simulations have also investigated column density with (Hummels et al. 2013) created adaptive mesh refinement (AMR) simulations of the CGM with various feedback strengths, post-processing column density and comparing to observations. Their column density of Mg II and O VI under-predicts observations above $r > 50 \text{ kpc}$, with some agreement for Mg II at $r < 50 \text{ kpc}$. We find more reliable agreement between our simulations and observations out to larger radii but only for haloes with mass $\geq 10^{11} M_\odot$. Our simulations below this mass match at very low radii with observations extending to the virial radius. Our simulations also find good agreement between simulations and observations for haloes with a mass $\geq 10^{11} M_\odot$.

5 CONCLUSION

We have investigated the physical and observational properties of a sample of CGM haloes from the Auriga suite of cosmological simulations. These haloes were within a mass range of $10^{10} < M_{200c} < 10^{12.5}$. We analysed the temperature, density, metallicity and radial velocity as a function of M_{200c} and R_{200c} as well as investigating the column density of H I, C IV, O VI, Mg II and Si II as a function of M_\star and R_{200c} , comparing our simulations to observations. This data was used to better understand how changing the M_{200c} of the CGM affects the scatter of its properties. Our main results from this study are as follows:

- $M_{200c} > 10^{9.5} M_\odot$ and $< 10^{12.5} \text{ K}$ begin accreting cool (10^4 K) matter onto the centre of the CGM which indicates a shorter cooling time than free fall time meaning these galaxies are undergoing an isothermal shock. As the M_{200c} increases, we notice the median temperature and density increasing as well as their scatter. We conclude from this that the multiphase nature of the CGM is therefore M_{200c} dependent, meaning more phases are present in the gas with increasing M_{200c} . We also see this radially, with the median and range of temperature in the outer CGM increasing the higher in M_{200c} .
- Metallicity decreases in scatter for haloes of higher M_{200c} ($> 10^{9.5} M_\odot$). The stellar population of these galaxies is much higher with heavier stars meaning they are producing heavier elements, thus causing an increase in the overall metallicity. Larger scatter in temperatures also leads to more metals surviving in the outer CGM which we see radially. These metals reach so far out because of stronger feedback from more massive galaxies.
- H I is ubiquitous throughout our haloes with median and scatter values within the margin of observations across a wide range of stellar masses and radial bins. We find a high concentration of H I in the centre of our haloes, decreasing to a plateau of 10^{14} cm^{-2} at larger radii. Our simulations over-predict H I on average in the central $0.125 R_{200c}$ when compared to observations.
- In the warm regime, C IV and O VI column densities from our simulations agrees with observations at high M_\star and low R_{200c} (row 2 and 3 of Figure 7 and 6). Average C IV scales linearly with M_\star for $R < 0.0125 R_{200c}$ but decreases for low mass haloes as radius increases. O VI only matches observations at high M_\star with intermediate M_\star ($10^8 - 10^{9.7} M_\odot$) showing our lowest column density values. With

median temperature being consistently 10^4 K in this mass range, it is understandable why the O VI readings would be so low. In addition, it is only past $M_\star = 10^{9.7} M_\odot$ that we see a sharp increase in O VI column density, at the same point we see an increase in temperature scatter to above 10^5 K .

- Finally in the cool regime, Mg II and Si II column densities are found to be high in the centres of haloes as these species trace 10^4 K gas. Accreting gas in haloes with $M_{200c} \geq 10^{9.5} M_\odot$ would have largely cold gas inflowing towards the centre as the cooling time is shorter than the free fall time. Mg II and Si II therefore survive in lower mass haloes near the centre of the CGM. As M_{200c} increase, stronger outflows will cause these species to reach higher radii but they won't survive at these temperatures. Conversely, haloes with mass of order $< 10^{10.5}$ do not have sufficiently strong outflows to extend Mg II and Si II to the outer CGM.

ACKNOWLEDGEMENTS

DATA AVAILABILITY

Simulation data is available upon reasonable request.

REFERENCES

- Anderson M. E., Bregman J. N., 2010, *ApJ*, **714**, 320
 Appleby S., Davé R., Sorini D., Cui W., Christiansen J., 2023, *MNRAS*, **519**, 5514
 Booth C. M., Schaye J., 2009, *MNRAS*, **398**, 53
 Bordoloi R., et al., 2014, *ApJ*, **796**, 136
 Butsky I. S., et al., 2022, *ApJ*, **935**, 69
 Cedrés B., et al., 2021, *ApJ*, **915**, L17
 Cen R., Ostriker J. P., 1999, *ApJ*, **514**, 1
 Chen Z.-F., Qin H.-C., Cai J.-T., Zhou Y.-T., Chen Z.-G., Pang T.-T., Wang Z.-W., Cheng K.-F., 2023, *ApJS*, **265**, 46
 Cottle J. N., Scannapieco E., Brüggen M., 2018, *ApJ*, **864**, 96
 Davis M., Efstathiou G., Frenk C. S., White S. D. M., 1985, *ApJ*, **292**, 371
 Eisenreich M., Naab T., Choi E., Ostriker J. P., Emsellem E., 2017, *MNRAS*, **468**, 751
 Faerman Y., Werk J. K., 2023, *arXiv e-prints*, p. arXiv:2302.00692
 Faucher-Giguere C.-A., Oh S. P., 2023, *arXiv e-prints*, p. arXiv:2301.10253
 Faucher-Giguere C.-A., Lidz A., Zaldarriaga M., Hernquist L., 2009, *ApJ*, **703**, 1416
 Ferland G. J., et al., 2017, *Rev. Mex. Astron. Astrofis.*, **53**, 385
 Fox A. J., Wakker B. P., Savage B. D., Tripp T. M., Sembach K. R., Bland-Hawthorn J., 2005, *ApJ*, **630**, 332
 Girelli G., Pozzetti L., Bolzonella M., Giocoli C., Marulli F., Baldi M., 2020, *A&A*, **634**, A135
 Grand R. J. J., et al., 2017, *MNRAS*, **467**, 179
 Hafen Z., et al., 2020, *MNRAS*, **494**, 3581
 Hummels C. B., Bryan G. L., Smith B. D., Turk M. J., 2013, *MNRAS*, **430**, 1548
 Hummels C. B., Smith B. D., Silvia D. W., 2017, *ApJ*, **847**, 59
 Johnson S. D., Chen H.-W., Mulchaey J. S., 2015, *MNRAS*, **449**, 3263
 Kimm T., Bieri R., Geen S., Rosdahl J., Blaizot J., Michel-Dansac L., Garel T., 2022, *ApJS*, **259**, 21
 Kraemer S. B., et al., 2005, *ApJ*, **633**, 693
 Lehner N., Howk J. C., Wakker B. P., 2015, *ApJ*, **804**, 79
 Lopez L. A., Mathur S., Nguyen D. D., Thompson T. A., Olivier G. M., 2020, *ApJ*, **904**, 152
 Machado R. E. G., Tissera P. B., Lima Neto G. B., Sodré L., 2018, *A&A*, **609**, A66
 Mathur S., Gupta A., Das S., Kronegold Y., Nicastro F., 2021, *ApJ*, **908**, 69
 Mina M., Shen S., Keller B. W., Mayer L., Madau P., Wadsley J., 2021, *A&A*, **655**, A22

- Moster B. P., Somerville R. S., Maulbetsch C., van den Bosch F. C., Macciò A. V., Naab T., Oser L., 2010, [ApJ](#), **710**, 903
- Nelson D., Byrohl C., Peroux C., Rubin K. H. R., Burchett J. N., 2021, [MNRAS](#), **507**, 4445
- Nelson D., et al., 2023, [MNRAS](#), **522**, 3665
- Okamoto T., Gao L., Theuns T., 2008, [MNRAS](#), **390**, 920
- Oppenheimer B. D., Davé R., Kereš D., Fardal M., Katz N., Kollmeier J. A., Weinberg D. H., 2010, [MNRAS](#), **406**, 2325
- Pakmor R., Springel V., Bauer A., Mocz P., Muñoz D. J., Ohlmann S. T., Schaal K., Zhu C., 2016, [MNRAS](#), **455**, 1134
- Peeples M. S., Werk J. K., Tumlinson J., Oppenheimer B. D., Prochaska J. X., Katz N., Weinberg D. H., 2014, [ApJ](#), **786**, 54
- Pillepich A., et al., 2018, [MNRAS](#), **473**, 4077
- Planck Collaboration et al., 2014, [A&A](#), **571**, A16
- Prochaska J. X., et al., 2017, [ApJ](#), **837**, 169
- Putman M. E., Peek J. E. G., Joung M. R., 2012, [ARA&A](#), **50**, 491
- Qu Z., et al., 2022, [MNRAS](#), **516**, 4882
- Rahmati A., Pawlik A. H., Raičević M., Schaye J., 2013, [MNRAS](#), **430**, 2427
- Ramesh R., Nelson D., Pillepich A., 2023, [MNRAS](#), **518**, 5754
- Ranjan A., et al., 2022, [A&A](#), **661**, A134
- Rubin K. H. R., Prochaska J. X., Koo D. C., Phillips A. C., 2012, [ApJ](#), **747**, L26
- Schaye J., et al., 2015, [MNRAS](#), **446**, 521
- Springel V., 2010, [MNRAS](#), **401**, 791
- Springel V., Hernquist L., 2003, [MNRAS](#), **339**, 289
- Strawn C., Roca-Fàbregas S., Primack J., 2023, [MNRAS](#), **519**, 1
- Suresh J., Rubin K. H. R., Kannan R., Werk J. K., Hernquist L., Vogelsberger M., 2017, [MNRAS](#), **465**, 2966
- Trebitsch M., Blaizot J., Rosdahl J., Devriendt J., Slyz A., 2017, [MNRAS](#), **470**, 224
- Truong N., et al., 2023, arXiv e-prints, p. arXiv:2307.01277
- Tumlinson J., et al., 2013, [ApJ](#), **777**, 59
- Tumlinson J., Peeples M. S., Werk J. K., 2017, [ARA&A](#), **55**, 389
- Vogelsberger M., Genel S., Sijacki D., Torrey P., Springel V., Hernquist L., 2013, [MNRAS](#), **436**, 3031
- Wang L., Dutton A. A., Stinson G. S., Macciò A. V., Penzo C., Kang X., Keller B. W., Wadsley J., 2015, [MNRAS](#), **454**, 83
- Werk J. K., Prochaska J. X., Thom C., Tumlinson J., Tripp T. M., O'Meara J. M., Peeples M. S., 2013, [ApJS](#), **204**, 17
- Werk J. K., et al., 2014, [ApJ](#), **792**, 8
- Werk J. K., et al., 2016, [ApJ](#), **833**, 54
- Wright R. J., Lagos C. d. P., Power C., Correa C. A., 2021, [MNRAS](#), **504**, 5702
- Zahedy F. S., Chen H.-W., Johnson S. D., Pierce R. M., Rauch M., Huang Y.-H., Weiner B. J., Gauthier J.-R., 2019, [MNRAS](#), **484**, 2257
- Zheng Y., et al., 2023, arXiv e-prints, p. arXiv:2301.12233

APPENDIX A: COLLATED HALO PROPERTIES

We present here tabulated data from our selection of haloes. This data outlines key properties of the largest haloes within our FoF region.

This paper has been typeset from a $\text{\TeX}/\text{\LaTeX}$ file prepared by the author.

Halo Name ^a	$\log_{10} M_{200c}^b (M_\odot)$	$\log_{10} T_{200c}^c (K)$	$R_{200c}^d (kpc)$	$\log_{10} M_\star^e (M_\odot)$	SFR ^f (M_\odot/yr)
Au0_10	10.0	4.36	45.6	7.94	0.00
Au1_10	9.75	4.04	37.5	4.92	0.00
Au2_10	10.7	4.84	76.7	9.46	0.46
Au3_10	9.78	4.14	38.4	6.44	0.00
Au4_10	9.62	3.98	33.9	5.67	0.00
Au5_10	9.71	4.12	36.3	7.10	0.00
Au6_10	10.4	4.62	61.0	8.95	0.09
Au7_10	9.64	4.05	34.5	6.51	0.00
Au8_10	10.1	4.47	49.2	8.88	0.05
Au9_10	10.6	4.79	70.1	9.05	0.16
Au10_10	9.78	4.08	38.9	6.26	0.00
Au11_10	10.4	4.66	62.1	8.72	0.07
Au12_10	9.85	4.28	40.5	8.05	0.00
Au13_10	9.65	4.11	34.6	7.19	0.00
<hr/>					
Au0_11	11.0	4.90	98.4	9.82	0.79
Au1_11	11.3	5.14	126	10.1	2.06
Au2_11	11.1	5.11	109	9.79	0.78
Au3_11	11.4	5.21	129	10.2	1.15
Au4_11	11.5	5.33	139	10.1	1.43
Au5_11	11.5	5.36	138	10.2	0.60
Au6_11	11.0	4.95	96.1	9.75	0.53
Au7_11	11.2	5.07	114	9.95	1.42
Au8_11	11.0	5.06	101	9.58	0.46
Au9_11	11.0	4.90	98.5	9.68	0.63
Au10_11	10.9	4.89	92.1	9.59	0.48
Au11_11	11.0	4.98	94.7	9.79	0.89
<hr/>					
AuL8_12	11.9	5.57	200	10.8	5.71
Au16_12	12.2	5.81	242	11.0	4.21
Au23_12	12.2	5.72	242	11.0	4.60
Au6_12	12.0	5.59	212	10.8	2.70

Table A1. Specific physical properties of our simulations. a) halo reference name b) M_{200} including all gas c) virial temperature d) virial radius of halo e) M_\star f) star formation rate.